International Journal of Mechanical Sciences 68 (2013) 47–55

Contents lists available at SciVerse ScienceDirect

International Journal of Mechanical Sciences

journal homepage: www.elsevier.com/locate/ijmecsci

Prediction of the mechanical properties of micro-lattice structures subjected to multi-axial loading

K. Ushijima [a,*], W.J. Cantwell [b], D.H. Chen [c]

[a] Department of Mechanical Engineering, Kyushu Sangyo University, Matsukadai 2-3-1, Higashi-ku, Fukuoka 8138503, Japan
[b] Department of Aerospace Engineering, Khalifa University of Science, Technology and Research (KUSTAR), Abu Dhabi, P.O. Box 127788, United Arab Emirates
[c] Department of Mechanical Engineering, Tokyo University of Science, Kagurazaka 1-3, Shinjuku-ku, Tokyo 1628601, Japan

ARTICLE INFO

Article history:
Received 9 June 2012
Received in revised form
13 October 2012
Accepted 18 December 2012
Available online 16 January 2013

Keywords:
Micro-lattice
Mechanical properties
Plastic collapse
FEM

ABSTRACT

The mechanical properties of micro-lattice structures subjected to a normal stress state are investigated using both a classical beam theory approach and the finite element technique. In particular, an approach for predicting the yield surface of lattice structures subjected to either a uniaxial or a biaxial stress state is proposed. In addition, the geometrical and material conditions for the occurrence of elastic buckling under a triaxial stress state are identified. The stiffness and plastic collapse strengths of the micro-lattice structures are compared with the corresponding properties of other lightweight structures. It is shown that micro-lattices offer significant potential for use in the design of lightweight cellular structures.

1. Introduction

For many years, lightweight structures such as honeycombs, foams and lattice structures have been widely used in the design of lightweight engineering structures as a result of their superior mechanical properties per unit volume. In recent years, a range of metallic foams have been produced for use as core materials in load-bearing sandwich panels, and studied by many researchers [1–13]. In the last decade, a number of manufacturing techniques, such as soft lithography in combination with electrochemical plating and welding, injection molding, investment casting, brazing, and rapid prototyping have been used to produce lattice structures with length scales ranging from millimetres to tens of centimetres [14–22].

Recent work at the University of Liverpool has investigated the use of the rapid prototyping manufacturing process of selective laser melting (SLM) to produce lattice structures with length dimensions at the micro-scale. Here, fine metallic powder (with particle diameters in the range of 15–30 μm) is selectively melted to form micro-struts with diameters of the order of 200 μm.

Fig. 1(a) shows a typical micro-lattice block, termed a body centred cubic, *BCC*, structure. This block consists of periodic cells in a scaffold-like structure, in which each cell is based on a number of truss elements or beams connected to each other. Further details of the manufacturing technique and resulting structures are given by Mines [21]. Given that the SLM manufacturing technique can be used to manufacture a large number of possible micro-lattice configurations, there is a need to develop analysis methodologies to identify and develop optimal configurations.

Clearly, the mechanical properties of a lattice depend strongly on the micro-architecture of the structure. Deshpande et al. [4] investigated the topological criteria that dictate the deformation mechanisms in cellular solids by analysing the rigidity of pin-jointed frameworks comprising inextensional struts. It was shown that stretching-dominated lattice materials are generally much stiffer than their bending-dominated counterparts. The authors identified the minimum node connectivity for a special class of lattices in stretching-dominated 2D and 3D structures.

Ushijima et al. [12,13] used numerical, experimental and analytical approaches to investigate the mechanical properties of stainless steel *BCC* micro-lattice blocks under uniaxial compressive and transverse shear loading. Applying Deshpande et al.'s analysis [4], it can be shown that the *BCC* structure is a bending-dominated structure, indicating that it is a weight-inefficient structure. If the *BCC* structure is subjected to a uniaxial normal stress σ_x or σ_y or σ_z, the strands will deform predominantly in bending, and the resulting mechanical properties, such as initial stiffness and plastic yielding strength are much lower than those for other stretching-dominated structures. However, it is natural that the deformation mode depends strongly on the nature of applied load. For example, if the *BCC* structure is subjected to biaxial or triaxial loading, the individual strut would be subjected to axial loading, with the effect that the structure becomes much stiffer than expected. Given that the plastic yielding behaviour of the *BCC* structure under multiaxial loading is not understood, the

* Corresponding author. Tel.: +81 926735605; fax: +81 926735090.
E-mail addresses: kuniharu@ip.kyusan-u.ac.jp (K. Ushijima), wesley.cantwell@kustar.ac.ae (W.J. Cantwell), chend@rs.kagu.tus.ac.jp (D.H. Chen).

0020-7403/$ - see front matter © 2013 Elsevier Ltd. All rights reserved.
http://dx.doi.org/10.1016/j.ijmecsci.2012.12.017

mechanical properties of the *BCC* structure under bi- or triaxial stress state need to be investigated.

In this paper, analytical and numerical techniques are used to predict the mechanical properties of *BCC* micro-lattice structure with various angles between the adjacent strands subjected to multi-axial loadings. In particular, the plastic yield surface under biaxial loading and the occurrence of elastic buckling prior to plastic yielding under triaxial loading are discussed.

2. Numerical procedure

2.1. Description of the micro-structure and definition of the relative density

Fig. 1(b) and (c) shows the geometry of the unit-cell of the *BCC* lattice structure. The unit-cell consists of eight strands having the same length, L, connected to each other. The cross-section of each strand is assumed to be circular, having a constant diameter d. The angles between adjacent strands are described by the three parameters γ_x, γ_y, and γ_z. Three additional angles θ_x, θ_y and θ_z are introduced in order to enable the mechanical properties (i.e. the initial stiffness, Poisson's ratio and the plastic collapse strength in the three directions) to be expressed in a simple form. These angles are determined as follows:

$$\begin{cases} \theta_x = \angle HAD = \angle GBC, & \theta_y = \angle CAB = \angle GEF, & \theta_z = \angle EAF = \angle HDG, \\ \gamma_x = \angle OAB = \angle OBA, & \gamma_y = \angle OAE = \angle OEA, & \gamma_z = \angle OAD = \angle ODA. \end{cases} \tag{1}$$

Also, by adopting the above definitions, the following equations can be shown to apply:

$$\begin{cases} \cos^2\gamma_x + \cos^2\gamma_y + \cos^2\gamma_z = 1, \\ \tan\theta_x = \dfrac{\cos\gamma_y}{\cos\gamma_z}, \quad \tan\theta_y = \dfrac{\cos\gamma_z}{\cos\gamma_x}, \quad \tan\theta_z = \dfrac{\cos\gamma_x}{\cos\gamma_y}. \end{cases} \tag{2}$$

BCC lattice structures based on various combinations of L, γ_x, γ_y, and γ_z can be fabricated using the selective laser melting technique. Here, the width L_x, height L_y and depth L_z of the unit-cell can be written in terms of the angles γ_x, γ_y, and γ_z and the length of an individual strand L as follows:

$$L_x = 2L\cos\gamma_x, \quad L_y = 2L\cos\gamma_y, \quad L_z = 2L\cos\gamma_z. \tag{3}$$

When considering the mechanical properties of the micro-lattice structures, it is generally appropriate to determine their specific properties by dividing the appropriate property by the associated density of the lattice. Here, the relative density of the *BCC* lattice

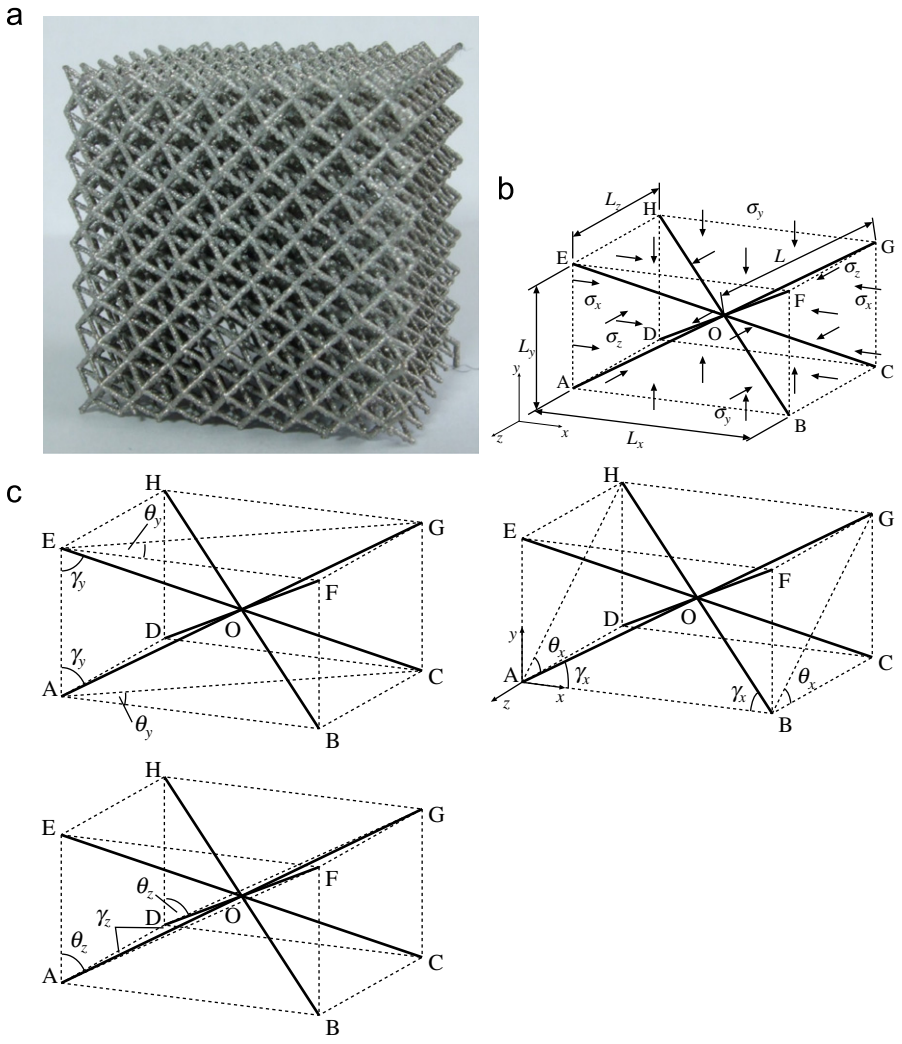

Fig. 1. (a) Overall shape of the *BCC* lattice block (a 20 mm cube), (b) geometries and loading condition for a representative unit-cell and (c) definition of angles θ_x, θ_y, θ_z, γ_x, γ_y. γ_z for a unit-cell.

material $\overline{\rho}$ is given by

$$\overline{\rho} = \frac{2\pi d^2 L}{L_x L_y L_z} = \left(\frac{d}{L}\right)^2 \cdot \frac{\pi}{4\cos\gamma_x \cos\gamma_y \cos\gamma_z}. \quad (4)$$

The above parameter $\overline{\rho}$ is only valid for small densities, because the volume of material associated with the joints is not taken into account. In addition, the classical beam theory approach adopted in this paper is only applicable at relatively small densities. The effect of the volume of the joints on the mechanical properties of the *BCC*, using a FE analysis based on 1D beam and 3D solid elements, has been discussed in a previous paper [12]. In this paper, the mechanical properties of *BCC* lattice structures are discussed for densities up to 0.1. The resulting values are then compared with those of other lightweight structures.

2.2. Assumptions

A number of assumptions are made during the development of the following micro-lattice models. Firstly, the material is assumed to obey an isotropic, multi-linear stress–strain relationship, similar to that for stainless steel 316L. This stress–strain curve was obtained from a tensile test on a micro-strut [11]. Here, Young's modulus, E_s, the yield stress, σ_{ys}, and Poisson's ratio, ν, for stainless steel 316L were taken as 140 GPa, 143.6 MPa and 0.3, respectively. Also, the compressive and tensile stress–strain relationships are assumed to be the same. Secondly, it is assumed that the strand can be deformed in axial tension, compression and bending. The effect of torsion is assumed to be negligible. Also, according to the Euler–Bernoulli assumption, the bending strain, ε, is assumed to be linearly distributed over the cross-section, and given by

$$\varepsilon = \kappa\eta, \quad (5)$$

where κ is the curvature, and η is the distance from the neutral axis.

2.3. Conventional beam theory analysis

In this section, a theoretical approach for predicting the aforementioned mechanical properties (initial stiffness, Poisson's ratio and plastic collapse strength) of lattice structures subjected to normal stresses σ_x, σ_y and σ_z is introduced. The shear response of lattice structures has been discussed in a previous study [13]. As a result of symmetry, the cantilever beam model shown in Fig. 2 is used, instead of a unit-cell model. Here, the movement of point A relative to point O in the *xyz* coordinate system can be determined using the unknown displacements u, v and w. Also, a new coordinate system $x_2y_2z_2$ is introduced by applying a rotation transformation to the *xyz* coordinate system. The unknown displacements along the x_2-, y_2- and z_2-directions are termed u_2, v_2 and w_2, respectively.

Moreover, in this study, the angles θ_x, θ_y and θ_z are used for the *BCC* lattice under a uniaxial stress σ_x, σ_y and σ_z, respectively, in order to describe the mechanical properties in a simple form.

2.3.1. General expressions for the mechanical properties of a BCC lattice under a uniaxial stress state

In an earlier study [12], the authors developed an approach for predicting the initial stiffness and plastic collapse strength of a cubic unit-cell structure (L_x=L_y=L_z). Here, the same approach was used to develop general expressions for the mechanical properties of a *BCC* lattice with arbitrary lengths L_x, L_y and L_z will be developed in this section.

Firstly, a theoretical approach for a lattice structure subjected to a uniaxial stress σ_x is considered. When considering the mechanical properties under the action of a stress σ_x in the *x*-direction, the angles γ_x and θ_x are used in the rotational transformation between *xyz* and $x_2y_2z_2$ coordinate systems, as shown in Fig. 3. The relationship between (u_2, v_2, w_2) and (u,v,w) under a stress σ_x can be written as

$$\begin{pmatrix} u_2 \\ v_2 \\ w_2 \end{pmatrix} = \begin{pmatrix} \cos\gamma_x & \sin\gamma_x \sin\theta_x & -\sin\gamma_x \cos\theta_x \\ 0 & \cos\theta_x & \sin\theta_x \\ \sin\gamma_x & -\cos\gamma_x \sin\theta_x & -\cos\gamma_x \cos\theta_x \end{pmatrix} \begin{pmatrix} u \\ v \\ w \end{pmatrix}. \quad (6)$$

The cantilever beam OA, subjected to the stress σ_x, will deform in the ABGH plane as shown in Fig. 1(c). That is, by using the coordinate system $x_2y_2z_2$, as shown in Fig. 3, the beam can be considered as deforming in the z_2-direction only, i.e. $w_2 \neq 0$ and u_2=v_2=0. Therefore, the following relationships between u, v and w can be derived from Eq. (6):

$$u = \frac{\tan\gamma_x}{\cos\theta_x} w, \quad v = -w\tan\theta_x. \quad (7)$$

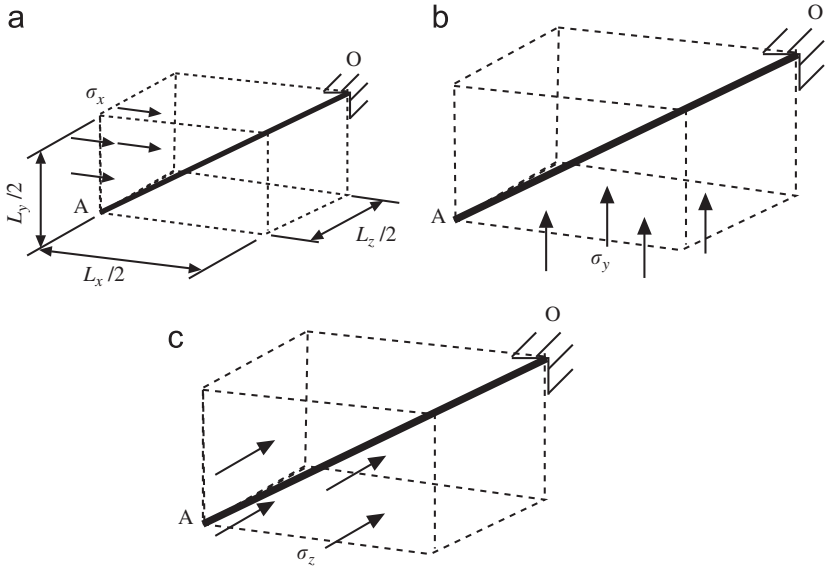

Fig. 2. Three stress conditions for a cantilever beam OA (a) under σ_x, (b) under σ_y and (c) under σ_z.

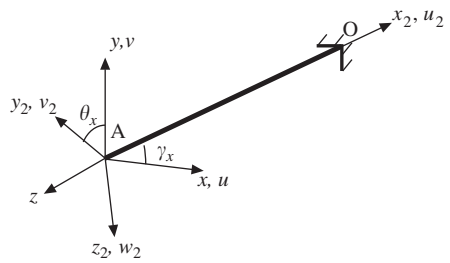

Fig. 3. Relationship between the two coordinate systems xyz and $x_2y_2z_2$ for a strand OA under a stress σ_x in the x-direction.

Also from Eqs. (6) and (7), the displacement w_2 in the z_2-direction can be written in terms of w as

$$w_2 = \frac{w}{\cos\gamma_x \cos\theta_x}. \tag{8}$$

Given that the beam OA deforms in the ABGH plane, the strand can be considered as being subjected to a shear force, F_{z2} in the z_2-direction and a bending moment M_{y2} around the y_2-axis. The force and associated bending moment can be expressed in terms of the unknown displacement w_2 as

$$F_{z2} = \frac{12E_sI}{L^3}w_2, \quad M_{y2} = \frac{F_{z2}L}{2} = \frac{6E_sI}{L^2}w_2, \tag{9}$$

where I is the moment of inertia for a single strand ($=\pi d^4/64$). As noted previously [12], the unknown displacements (u,v,w) or (u_2,v_2,w_2) can be obtained by considering the condition of equilibrium between the stored strain energy and the external work for a cantilever beam. Here, the procedure will be explained briefly.

The elastic strain energy U of a beam OA subjected to a stress σ_x can be written in terms of the unknown displacement w as

$$U = \frac{1}{2E_sI_s}\int_0^L (M_{y2} - F_{z2}s)^2\,\mathrm{d}s = \frac{6E_sI_sw^2}{L^3\cos^2\gamma_x\cos^2\theta_x}. \tag{10}$$

Also, the external work Q done by the applied stress σ_x can be shown to be

$$Q = \sigma_x \cdot \frac{L_y}{2}\cdot\frac{L_z}{2}u = \sigma_xL^2w\cdot\frac{\tan\gamma_x\cos\gamma_y\cos\gamma_z}{\cos\theta_x}. \tag{11}$$

Following the work by Zhu et al. [2], the unknown displacement w can be obtained by applying Love's theory [23] of the potential energy for an elastic body. The deformation potential energy V for a beam is determined by the difference between Q and U, and can be expressed as a function of the displacement w and stress σ_x as

$$V = Q - U = \sigma_xL^2w\cdot\frac{\tan\gamma_x\cos\gamma_y\cos\gamma_z}{\cos\theta_x} - \frac{6E_sI_sw^2}{L^3\cos^2\gamma_x\cos^2\theta_x}. \tag{12}$$

According to Love's theorem of minimum potential energy [23], the unknown displacement w yields a minimum value for the potential energy V, i.e.:

$$\frac{\partial V}{\partial w} = 0. \tag{13}$$

By substituting Eq. (12) into Eq. (13), the displacement w can be shown to be

$$w = \frac{8\sigma_xL^5}{3E_s\pi d^4}\cdot\sin 2\gamma_x\cos\gamma_y\cos\gamma_z\cos\theta_x. \tag{14}$$

Also, the displacements u and v in x- and y-directions can be obtained from Eqs. (7) and (14) as

$$\begin{cases} u = \dfrac{16\sigma_xL^5}{3E_s\pi d^4}\cdot\sin^2\gamma_x\cos\gamma_y\cos\gamma_z, \\ v = -\dfrac{8\sigma_xL^5}{3E_s\pi d^4}\cdot\sin 2\gamma_x\cos\gamma_y\cos\gamma_z\sin\theta_x. \end{cases} \tag{15}$$

Finally, the initial stiffness, E_x^*, and the two Poisson's ratios, v_{xy} and v_{xz}, are given as

$$\begin{cases} E_x^* = \dfrac{\sigma_x}{(2u/L_x)} = \dfrac{3\pi E_s}{16}\cdot\left(\dfrac{d}{L}\right)^4\cdot\dfrac{\cos\gamma_x}{\sin^2\gamma_x\cos\gamma_y\cos\gamma_z}, \\ v_{xy}^* = \left|\dfrac{\varepsilon_y}{\varepsilon_x}\right| = \dfrac{\cos^2\gamma_x\sin\theta_x}{\sin\gamma_x\cos\gamma_y}, \\ v_{xz}^* = \left|\dfrac{\varepsilon_z}{\varepsilon_x}\right| = \dfrac{\cos^2\gamma_x\cos\theta_x}{\sin\gamma_x\cos\gamma_z} = v_{xy}^*. \end{cases} \tag{16}$$

Next, consider the plastic collapse strength of this *BCC* structure when subjected to a uniaxial stress σ_x. The maximum bending moment for the beam OA, i.e. $M_{max,x}$ occurs at the junction point O. Using Eqs. (8), (9) and (14), this can be written as

$$M_{max,x} = M_{y2} = \frac{\sigma_xL^3}{2}\sin\gamma_x\cos\gamma_y\cos\gamma_z. \tag{17}$$

Here, based on the same approach adopted in the earlier paper, the plastic collapse strength can be determined when the maximum bending moment reaches the fully plastic moment $M_p(=\sigma_{ys}d^3/6)$ of a strand, i.e.:

$$\sigma_{x,pl}^* = \frac{\sigma_{ys}}{3}\cdot\left(\frac{d}{L}\right)^3\cdot\frac{1}{\sin\gamma_x\cos\gamma_y\cos\gamma_z}. \tag{18}$$

Similarly, the mechanical properties of a lattice structure subjected to normal stress either σ_y or σ_z can be derived using this approach. Here, the relationship between (u_2,v_2,w_2) and (u,v,w) under the application of a stress σ_y according to Eq. (6) is used as follows:

$$\begin{pmatrix} u_2 \\ v_2 \\ w_2 \end{pmatrix} = \begin{pmatrix} \sin\gamma_y\cos\theta_y & \cos\gamma_y & -\sin\gamma_y\cos\theta_y \\ -\cos\gamma_y\cos\theta_y & \sin\gamma_y & \cos\gamma_y\sin\theta_y \\ \sin\theta_y & 0 & \cos\theta_y \end{pmatrix}\begin{pmatrix} u \\ v \\ w \end{pmatrix}. \tag{19}$$

Similarly, the relationship between (u_2,v_2,w_2) and (u,v,w) under the action of a stress σ_z is

$$\begin{pmatrix} u_2 \\ v_2 \\ w_2 \end{pmatrix} = \begin{pmatrix} \sin\gamma_z\sin\theta_z & \sin\gamma_z\cos\theta_z & -\cos\gamma_z \\ -\cos\theta_z & \sin\theta_z & 0 \\ \cos\gamma_z\sin\theta_z & \cos\gamma_z\cos\theta_z & \sin\gamma_z \end{pmatrix}\begin{pmatrix} u \\ v \\ w \end{pmatrix}. \tag{20}$$

Using above relationships, the problem of a beam OA, subjected to a stress σ_y or σ_z, can be regarded as a bending problem in a similar way to that previously adopted for the stress σ_x. The calculation procedure for determining the mechanical properties under the application of stresses σ_y or σ_z is equivalent to that used for the case of σ_x. Therefore, it can be shown that under the action of a stress σ_y:

$$\begin{cases} E_y^* = \dfrac{\sigma_y}{(2v/L_y)} = \dfrac{3\pi E_s}{16}\cdot\left(\dfrac{d}{L}\right)^4\cdot\dfrac{\cos\gamma_y}{\sin^2\gamma_y\cos\gamma_x\cos\gamma_z}, \\ v_{yz}^* = \left|\dfrac{\varepsilon_z}{\varepsilon_y}\right| = \dfrac{\cos^2\gamma_y\sin\theta_y}{\sin\gamma_y\cos\gamma_z}, \\ v_{yx}^* = \left|\dfrac{\varepsilon_x}{\varepsilon_y}\right| = \dfrac{\cos^2\gamma_y\cos\theta_y}{\sin\gamma_y\cos\gamma_x} = v_{yz}^*. \end{cases} \tag{21}$$

and similarly for σ_z:

$$\begin{cases} E_z^* = \dfrac{\sigma_z}{(2w/L_z)} = \dfrac{3\pi E_s}{16}\cdot\left(\dfrac{d}{L}\right)^4\cdot\dfrac{\cos\gamma_z}{\sin^2\gamma_z\cos\gamma_x\cos\gamma_y}, \\ v_{zx}^* = \left|\dfrac{\varepsilon_x}{\varepsilon_z}\right| = \dfrac{\cos^2\gamma_z\sin\theta_z}{\sin\gamma_z\cos\gamma_x}, \\ v_{zy}^* = \left|\dfrac{\varepsilon_y}{\varepsilon_z}\right| = \dfrac{\cos^2\gamma_z\cos\theta_z}{\sin\gamma_z\cos\gamma_y} = v_{zx}^*. \end{cases} \tag{22}$$

Using Eqs. (16), (21) and (22) the following relationships can be derived for the initial stiffnesses (E_x^*, E_y^*, E_z^*), and Poisson's ratios (ν_{xy}^*, ν_{xz}^*, ν_{yx}^*, ν_{yz}^*, ν_{zx}^*, ν_{zy}^*) in terms of the relative density $\overline{\rho}$:

$$\frac{\nu_{xy}^*}{E_x} = \frac{\nu_{xz}^*}{E_x} = \frac{\nu_{yx}^*}{E_y} = \frac{\nu_{yz}^*}{E_y} = \frac{\nu_{zx}^*}{E_z} = \frac{\nu_{zy}^*}{E_z} \cdot = \frac{4}{3E_s\overline{\rho}} \cdot \left(\frac{L}{d}\right)^2. \tag{23}$$

2.3.2. Mechanical properties under a biaxial stress state

When the *BCC* lattice structure is subjected to a biaxial stress field, the plastic yield surface can be derived from the results for the uniaxial stress conditions using the principle of superposition. As before, it is assumed that all the strands deform in a flexural mode. However, under biaxial loading, both the axial deformation and the bending deformation need be determined for each strand. Consider for example Fig. 4(a), in which the strand OA is subjected to biaxial stresses, σ_x and σ_y. The movements of a point A are termed u, v and w. It can be shown that the following is satisfied if no axial deformations occur within the strand:

$$(L\cos\gamma_x - u)^2 + (L\cos\gamma_y - v)^2 + (L\cos\gamma_z + w)^2 = L^2. \tag{24}$$

Here, the displacement w is subordinate to displacements u and v. Therefore, in order to satisfy the above equation, the independent parameters u and v should satisfy the following condition:

$$(L\cos\gamma_x - u)^2 + (L\cos\gamma_y - v)^2 \le L^2. \tag{25}$$

The above relationship between u and v can be visualized in Fig. 4(b). If the magnitude of the displacements u, v and w lie within each circle, only bending deformations occur within the strand. Also, as can be seen in Fig. 4(b), if the signs of the displacements u and v are negative, only axial deformation occurs. Here, we predict the plastic yield surface under biaxial loading conditions for bending-dominated conditions. The effect of axial, as well as bending deformations, on the yield surface will be reported in a subsequent paper. Here, the yield surface under a bending-dominated mode of deformation is predicted.

Assuming that the biaxial stresses, σ_x and σ_y, are applied to the lattice structure, the following equation based on the principle of superposition can be developed by equating the sum of the bending moments in an individual strand to the fully plastic moment M_p. When the strand OA is subjected to a normal stress of either σ_y or σ_z, the maximum moments at the junction point O, $M_{max,y}$ and $M_{max,z}$, can be expressed in terms of σ_y and σ_z as

$$\begin{cases} M_{max,y} = -\dfrac{\sigma_y L^3}{2}\cos\gamma_x \sin\gamma_y \cos\gamma_z, \\ M_{max,z} = \dfrac{\sigma_z L^3}{2}\cos\gamma_x \cos\gamma_y \sin\gamma_z. \end{cases} \tag{26}$$

Although the directions of these bending moments, shown in Eqs. (17) and (26), are different, they can be resolved into x-, y- and z-directions.

For the moment $M_{max,x}$ due to a stress σ_x, bending moments around x_2-, y_2- and z_2-axes can be shown using Eq. (6) that

$$\begin{pmatrix} M_{x2} \\ M_{y2} \\ M_{z2} \end{pmatrix} = \begin{pmatrix} 0 \\ M_{max,x}\cos\theta_x \\ M_{max,x}\sin\theta_x \end{pmatrix}. \tag{27}$$

Similarly, for the moment $M_{max,y}$ due to a stress σ_y, bending moments around x_2-, y_2- and z_2-axes can be shown that

$$\begin{pmatrix} M_{x2} \\ M_{y2} \\ M_{z2} \end{pmatrix} = \begin{pmatrix} M_{max,y}\sin\theta_y \\ 0 \\ M_{max,y}\cos\theta_y \end{pmatrix}. \tag{28}$$

Finally, for the moment $M_{max,z}$ due to a stress σ_z:

$$\begin{pmatrix} M_{x2} \\ M_{y2} \\ M_{z2} \end{pmatrix} = \begin{pmatrix} -M_{max,z}\cos\theta_z \\ M_{max,z}\sin\theta_z \\ 0 \end{pmatrix}. \tag{29}$$

The sum of the bending moments, M_m, under a biaxial stress state can be derived from Eqs. (27)–(29). For instance, the moment M_m resulting from the stresses σ_x and σ_y can be written as

$$M_m = \sqrt{M_{max,x}^2\cos^2\theta_x + M_{max,y}^2\sin^2\theta_y + 2M_{max,x}M_{max,y}\sin\theta_x\cos\theta_y}. \tag{30}$$

Therefore, the plastic yield surface for a *BCC* lattice under biaxial stresses σ_x and σ_y can be obtained by equating M_m to M_p, i.e.:

$$\sigma_{x,pl}^{*2}\sin^2\gamma_x\cos^2\gamma_y + \sigma_{y,pl}^{*2}\cos^2\gamma_x\sin^2\gamma_y - \frac{\sigma_{x,pl}^*\sigma_{y,pl}^*}{2}\sin 2\gamma_x \sin 2\gamma_y \sin\theta_x\cos\theta_y = \frac{\sigma_{ys}^2}{9\cos^2\gamma_z}\cdot\left(\frac{d}{L}\right)^6. \tag{31}$$

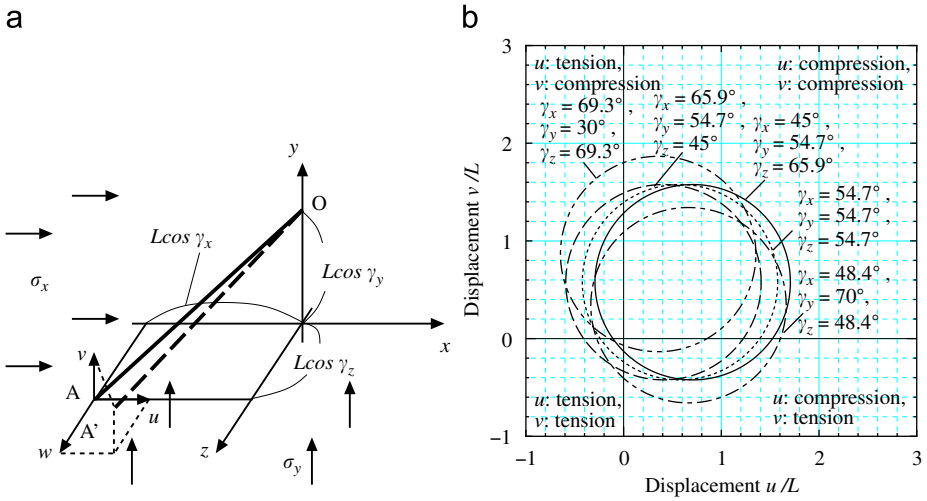

Fig. 4. Condition of displacements u and v for bending deformation under biaxial stresses σ_x and σ_y. (a) Schematic of movement at A under biaxial stresses and (b) bending-dominated condition for u and v.

Similarly, the yield surfaces under the stresses σ_y and σ_z, and also σ_z and σ_x can be derived in a similar manner, i.e.:

$$\sigma_{y,pl}^{*2}\sin^2\gamma_y\cos^2\gamma_z+\sigma_{z,pl}^{*2}\cos^2\gamma_y\sin^2\gamma_z+\frac{\sigma_{y,pl}^{*}\sigma_{z,pl}^{*}}{2}\sin 2\gamma_y\sin 2\gamma_z\sin\theta_y\cos\theta_z=\frac{\sigma_{ys}^2}{9\cos^2\gamma_x}\cdot\left(\frac{d}{L}\right)^6 \tag{32}$$

and

$$\sigma_{z,pl}^{*2}\sin^2\gamma_z\cos^2\gamma_x+\sigma_{x,pl}^{*2}\cos^2\gamma_z\sin^2\gamma_x-\frac{\sigma_{x,pl}^{*}\sigma_{z,pl}^{*}}{2}\sin 2\gamma_x\sin 2\gamma_z\sin\theta_z\cos\theta_x=\frac{\sigma_{ys}^2}{9\cos^2\gamma_y}\cdot\left(\frac{d}{L}\right)^6. \tag{33}$$

2.3.3. Pure stretching response under a triaxial stress state

When the *BCC* structure is subjected to a triaxial stress field, σ_x, σ_y and σ_z, axial deformations are inevitable. Therefore, the plastic yield surface under a triaxial stress state should be determined by considering the effects of bending and axial deformations simultaneously. As previously noted, the plastic yield surface under such combined deformations will be discussed in a subsequent paper. In the following, the condition of plastic yielding when all the strands deform axially (i.e., $u_2\neq 0$, $v_2=w_2=0$) will be discussed. In a subsequent section, we will consider the onset of elastic buckling by comparing the axial stress at plastic yielding with the value for the Euler buckling stress.

The axial force N on a beam OA, subjected to a triaxial stress state can be expressed as

$$N=\sigma_x\cdot\frac{L_yL_z}{4}\cdot\cos\gamma_x+\sigma_y\cdot\frac{L_xL_z}{4}\cdot\cos\gamma_y+\sigma_z\cdot\frac{L_xL_y}{4}\cdot\cos\gamma_z=(\sigma_x+\sigma_y+\sigma_z)\cdot L^2\cos\gamma_x\cos\gamma_y\cos\gamma_z. \tag{34}$$

Here, plastic yielding is deemed to occur when the axial force N reaches the fully plastic compressive force N_{pl}, i.e.:

$$N=N_{pl}=\frac{\pi d^2\sigma_{ys}}{4}. \tag{35}$$

Using Eqs. (4), (34) and (35), the sum of normal stresses at plastic yielding for a beam OA is given as

$$\sigma_{a,pl}^{*}=\sigma_{x,pl}^{*}+\sigma_{y,pl}^{*}+\sigma_{z,pl}^{*}=\left(\frac{d}{L}\right)^2\cdot\frac{\pi\sigma_{ys}}{4\cos\gamma_x\cos\gamma_y\cos\gamma_z}=\overline{\rho}\sigma_{ys}. \tag{36}$$

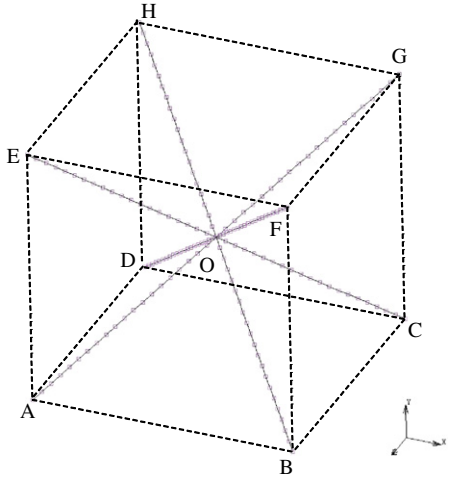

Fig. 5. Geometry of the finite element model.

2.4. Numerical analysis using FEM

In order to ascertain the accuracy of the theoretical predictions outlined in Section 2.3, a numerical analysis was conducted using the commercial FE software MSC.Marc. The assumptions associated with the FE model are discussed below.

Fig. 5 shows the unit-cell model adopted in the FE analysis. Each strand of the unit cell is composed of 20 beam elements (Element Number 98), and all elements are assumed to be homogeneous, isotropic and based on an elastoplastic material [24]. Given the symmetrical nature of the problem, periodicity displacement conditions are applied along all the edges of the model (A–H) using a link function that is readily available in the software package [24]. For example, the magnitudes of the x-direction displacements of points A, D, E and H were held constant.

3. Results and discussions

3.1. Estimation of mechanical properties (initial stiffness and Poisson's ratio) under a uniaxial stress state

Tables 1 and 2 show comparisons of the values of the initial stiffness and Poisson's ratio for various combinations of cell lengths L_x, L_y and L_z predicted by the theoretical and FE analyses. An examination of the tables shows that both sets of results agree for values of L_x, L_y and L_z. The data clearly show that the mechanical properties strongly depend on the length of the cell in the loading direction. For example,

Table 1
Comparisons of initial stiffness for various combinations of L_x, L_y and L_z.

L_x (mm)	L_y (mm)	L_z (mm)	E_x^* (MPa)		E_y^* (MPa)		E_z^* (MPa)	
			Theory	FEM	Theory	FEM	Theory	FEM
1.61	3.83	2.78	2.84	2.81	35.0	34.4	11.1	10.9
2.27	3.83	2.27	5.56	5.49	30.3	29.8	5.56	5.49
2.78	3.83	1.61	11.1	10.9	35.0	34.4	2.84	2.81
2.04	2.89	3.54	4.05	4.01	10.1	10.0	20.3	19.9
2.89	2.89	2.89	8.78	8.66	8.78	8.66	8.78	8.66
3.54	2.89	2.04	20.3	20.0	10.1	10.0	4.05	4.01
2.35	1.71	4.07	7.32	7.23	3.42	3.39	50.7	49.6
3.32	1.71	3.32	17.7	17.4	2.96	2.93	17.7	17.4
4.07	1.71	2.35	50.7	49.6	3.42	3.39	7.32	7.23

Table 2
Comparisons of Poisson's ratios for various combinations of L_x, L_y and L_z.

L_x (mm)	L_y (mm)	L_z (mm)	$\nu_{xy}^*=\nu_{xz}^*$		$\nu_{yz}^*=\nu_{yx}^*$		$\nu_{zx}^*=\nu_{zy}^*$	
			Theory	FEM	Theory	FEM	Theory	FEM
1.61	3.83	2.78	0.115	0.115	1.42	1.40	0.449	0.446
2.27	3.83	2.27	0.260	0.259	1.42	1.40	0.260	0.259
2.78	3.83	1.61	0.449	0.446	1.42	1.40	0.115	0.114
2.04	2.89	3.54	0.200	0.199	0.500	0.496	1.00	0.989
2.89	2.89	2.89	0.500	0.496	0.500	0.496	0.500	0.496
3.54	2.89	2.04	1.00	0.990	0.500	0.496	0.200	0.199
2.35	1.71	4.07	0.283	0.281	0.133	0.132	1.96	1.93
3.32	1.71	3.32	0.791	0.783	0.133	0.132	0.791	0.783
4.07	1.71	2.35	1.96	1.93	0.133	0.132	0.283	0.281

for the conditions considered here, the initial stiffness E_x^* is greatest when the value of the cell length L_x is largest (L_x=4.07).

3.2. Yield surface under biaxial stress state

Fig. 6(a) and (b) shows yield surfaces for a *BCC* structure with the same diameter-to-length ratio, d/L=0.08, subjected to biaxial stresses σ_x and σ_y. The lines in the figure correspond to the theoretical results given by Eq. (31), and the circular symbols to the FE data. Clearly, both sets of results agree with each other, and the yield surface becomes taller as the angle γ_x increases and γ_y decreases. That is, the plastic collapse induced by the stress σ_x increases for small values of γ_x, and the collapse induced by the stress σ_x increases for larger values of the angle γ_y. Also, it is evident in Tables 1 and 2 that the theoretical values are always greater than the FE results. This is due to the effect of axial deformation, an effect that was clearly evident in the FE analysis. When the length L_x becomes greater for the same value of length L_y, the axial deformation for all strands subjected to the normal stress σ_x is increased. As a result, the relative error in the values of E_x^* predicted by the FE results and beam theory becomes larger.

3.3. Values of stresses in three directions at plastic yielding under triaxial stress state

Fig. 7(a) and (b) shows the variation of the stresses $\sigma^*_{x,pl}$, $\sigma^*_{y,pl}$ and $\sigma^*_{z,pl}$ at plastic yielding obtained from the FEM analysis for various combinations of the angles γ_x, γ_y and γ_z under a triaxial stress state. Here, the displacements u, v and w are controlled in order to ensure that all the strands only deform axially. Also included in the figure are the theoretical results from Eq. (36), shown by dashed line. Fig. 7(a) and (b) shows that the stress values at plastic yielding, σ_x, σ_y and σ_z are strongly affected by the angles γ_x and γ_y, and if the angle γ_y is lower than 54.7°, the stress in y-direction is the highest among the three stresses, and if the angle γ_y is larger than 54.7°, the stress in y-direction is the lowest. Also, the hydraulic stress $\sigma^*_{a,pl}(=\sigma^*_{x,pl}+\sigma^*_{y,pl}+\sigma^*_{z,pl})$ remains almost constant regardless of angles γ_x and γ_y, and its value agrees well with the theoretical result obtained from Eq. (36).

3.4. Elastic buckling versus plastic yielding

In the previous section, we determined the stresses at plastic yielding when all the strands deform axially. If all strands are

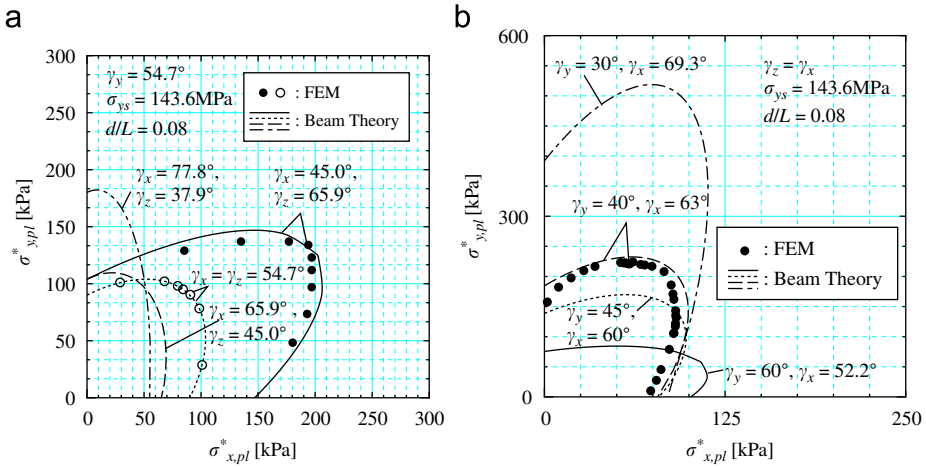

Fig. 6. Comparison of yield surface under biaxial stress σ_x and σ_y (a) by varying the angles γ_x and γ_z and (b) by varying the angle γ_y.

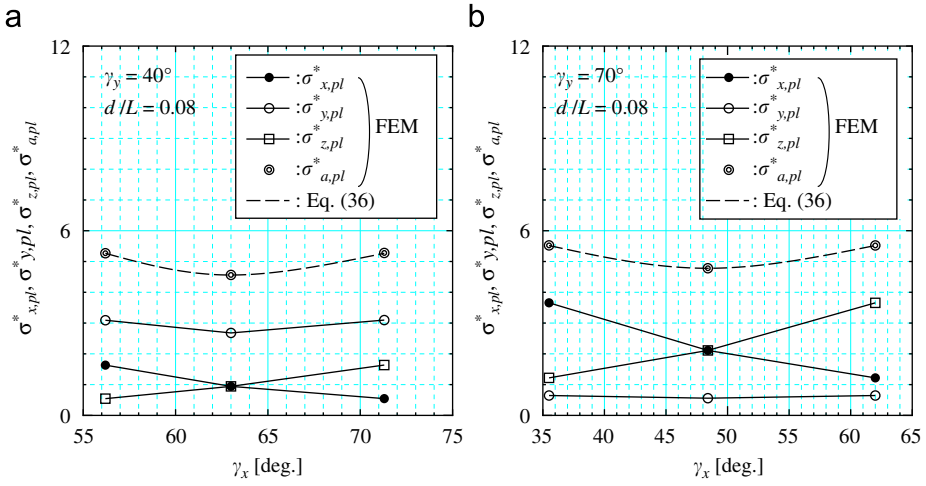

Fig. 7. Variation of stresses in three directions σ_x, σ_y and σ_z at the onset of plastic yielding (a) for angle γ_y=40° and (b) for angle γ_y=70°.

subjected to compressive stress in the axial direction, elastic buckling may be observed before plastic yielding. In order to clarify the occurrence condition of elastic buckling before plastic yielding, the axial peak load under triaxial stress state was calculated using FEM, and compared with the theoretical results for plastic yielding and elastic buckling. Here, the Euler buckling load [25] N_{cr} is given by

$$N_{cr} = \frac{n^2\pi^3 E_s d^4}{64L^2}. \tag{37}$$

Here, the factor n in Eq. (37) depends on the end constraints applied to the strands. In this paper, n is set to 2 (all degrees of freedoms are constrained). Also in the FE analysis, an imperfection whose shape is described by the following initial transverse deflection:

$$y_2 = \zeta \sin\left(\frac{\pi x_2}{L}\right) \tag{38}$$

is introduced in order to investigate collapse by elastic buckling. Here, ζ is the imperfection level, and a value of $\zeta = d/100$ was introduced into all strands. Also, x_2 and y_2 in Eq. (38) are the axial and the transverse directions in a strand as seen in Fig. 3.

Fig. 8 shows the variation of the axial peak load as a function of the yield stress σ_{ys}. The plastic yield load N_{pl} and the Euler buckling load N_{cr} are shown in the figure by solid and dotted lines, respectively. From the figure, one can distinguish the peak load induced by elastic buckling and that associated with plastic yielding. For example, for a lattice having an aspect ratio d/L=0.08, when the material's yield stress σ_{ys} is below 2 GPa, the peak loads obtained by FEM are proportional to the stress value, and close to the plastic compressive force N_{pl} given by Eq. (35). That is, plastic yielding is observed before elastic buckling while the material's yield stress σ_{ys} is below this value of 2 GPa. In contrast, when the yield stress is greater than 5 GPa, the peak loads obtained by FEM are virtually independent of the stress value. This indicates that elastic buckling occurs before plastic yielding while the material's yield stress σ_{ys} is greater than 5 GPa. This behaviour is virtually independent of the angles between adjacent strands γ_x, γ_y and γ_z, being principally dependent on the aspect ratio d/L.

Next, the material's yield stress was set to the value of 143.6 MPa determined from the stainless steel 316L stress–strain data. The peak loads for lattice structures based on a range of aspect ratios d/L were calculated, and are shown in Fig. 9. It is evident from Fig. 9 that if the lattice structure is based on stainless steel, elastic buckling occurs if the ratio of d/L is less than 0.02. As noted in the Introduction, strands with a diameter of the order of 0.2 mm can be readily manufactured using the rapid prototyping technique. Elastic buckling can be avoided if the length of the strand is less than 10 mm.

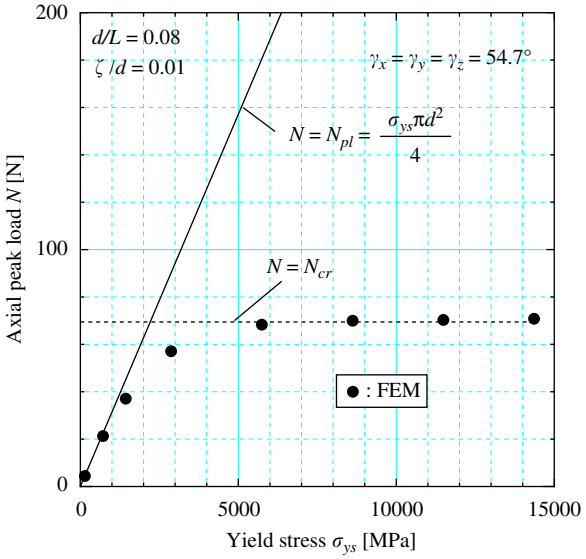

Fig. 8. The variation of the axial peak load N with yield stress σ_{ys}.

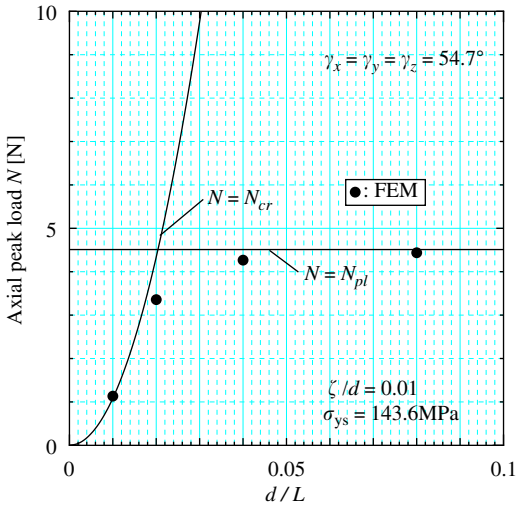

Fig. 9. The variation of the axial peak load with the diameter-to-length d/L ratio of the strand.

3.5. *Comparisons between the initial stiffness and plastic collapse strength for the micro-lattice structure and other lightweight structures*

In this section, the characteristics of the micro-lattice structure shown in Fig. 1(a) are compared with other lightweight structures.

Fig. 10(a) and (b) shows comparisons of the initial stiffness and plastic collapse strength for relative densities $\overline{\rho}$ in the range of 10^{-3} to 10^{-1}. In these figures, the mechanical properties of other lightweight structures (octet-truss and conventional metallic foams, Deshpande et al. [15]) are shown by the dotted and dashed curves. It can be seen from these figures that the lattice structure considered here offers the lowest material properties amongst these structures. In particular, the lattice offers a much lower stiffness than the octer-truss lattice (by a factor between 1/3000 and 1/30). This is due to the fact that the lattice is a so-called bending-dominated structure and the octet-truss structure is the stretching-dominated structure. In contrast, as for the plastic collapse strength, the lattice has a similar plastic collapse strength to conventional metallic foams. In contrast, as mentioned in a previous study [12], by using the selective laser melting technique, it is possible to manufacture a wide variety of micro-architectures. Fig. 11(a) and (b) shows examples of two possible types of unit cell used to develop micro-lattice structures (these are referred to as *BCCZ* and f_2*BCC* structures), and Fig. 11(c) shows a photograph of the *BCCZ* lattice block that has been manufactured using this technique. The *BCCZ* structure is similar to the *BCC* but with vertical pillars, and the f_2*BCC* structure is again based on the *BCC* with the addition of eight inclined strands across the faces of the *BCC* cube. The mechanical properties of the *BCCZ* and f_2*BCC* structures were also calculated by FEM and beam theory, and the resulting predictions are shown in Fig. 10(a) and (b). As can be seen from these figures, the mechanical properties are much higher than those for the *BCC*, and close to the values associated with the stretching-dominated octet-truss structure. This suggests that by changing the geometry of their micro-architecture, micro-lattice structures can be designed to offer significant potential for use in the design of lightweight cellular structures.

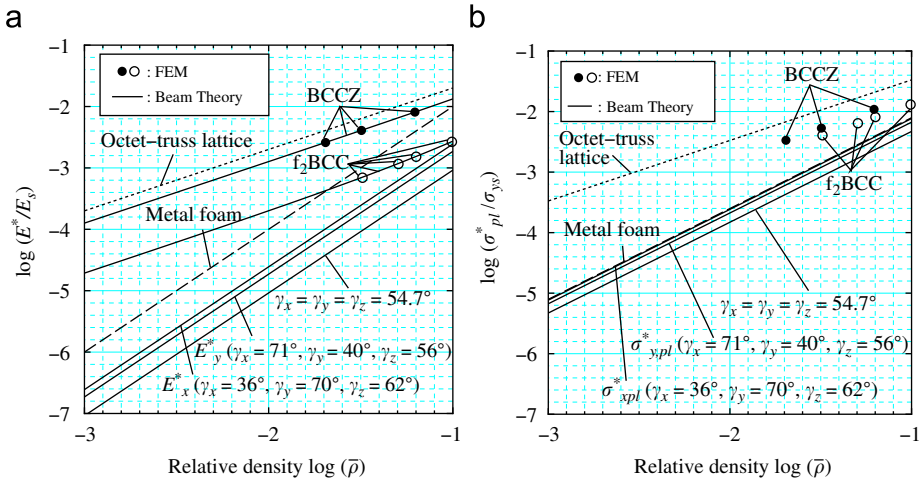

Fig. 10. Comparison of (a) the initial stiffness and (b) the plastic collapse strength for three types of lightweight structures.

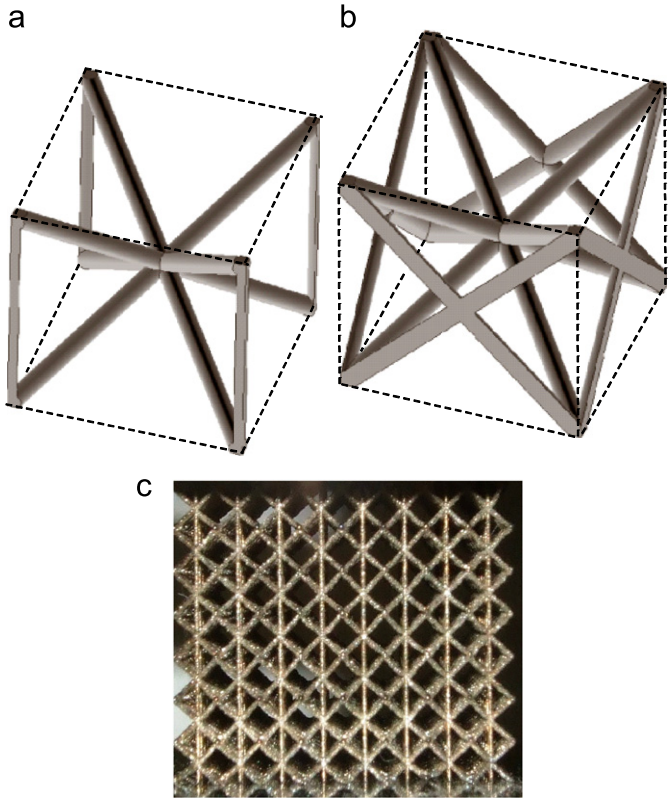

Fig. 11. Schematics of unit-cell for (a) *BCCZ* and (b) f_2BCC structures, and (c) photograph of *BCCZ* cube block manufactured by selective laser melting.

4. Conclusions

In this paper, the mechanical properties of micro-lattice structures based on various cell lengths and subjected to normal stresses in arbitrary directions are investigated using an analytical approach based on classical beam theory. The theoretical results agree well with the numerical results obtained by FEM. Also, the geometrical and material conditions for the occurrence of elastic buckling under a triaxial stress state are identified. Moreover, the stiffness and plastic collapse strength of the micro-lattice structures are compared with the corresponding properties of other lightweight structures, where it is shown that micro-lattices offer significant potential for use in the design of lightweight cellular structures.

References

[1] Gibson LJ, Ashby MF. Cellular solids: structure and properties. Cambridge: Cambridge University Press; 1997.
[2] Zhu HX, Knott JF, Mills NJ. Analysis of the elastic properties of open-cell foams with tetrakaidecahedral cells. J Mech Phys Solids 1997;45:319–43.
[3] Deshpande VS, Fleck NA. Isotropic constitutive models for metallic foams. J Mech Phys Solids 2000;48:1253–83.
[4] Deshpande VS, Ashby MF, Fleck NA. Foam topology bending versus stretching dominated architectures. Acta Mater 2001;49:1035–40.
[5] Wicks N, Hutchinson JW. Optimal truss plates. Int J Solids Struct 2001;38: 5165–83.
[6] Evans AG, Hutchinson JW, Fleck NA, Ashby MF, Wadley HNG. The topological design of multifunctional cellular materials. Progr Mater Sci 2001;46:309–27.
[7] Mohr D. Mechanism-based multi-surface plasticity model for ideal truss lattice materials. Int J Solids Struct 2005;42:3235–60.
[8] Sypeck DJ. Cellular truss core sandwich structures. Appl Compos Mater 2005;12:229–46.
[9] Xie LS, Chan KC. The effect of strut geometry on the yielding behaviour of open-cell foams. Int J Mech Sci 2006;48:249–55.
[10] McKown S, Shen Y, Brookes W, Cantwell WJ, Sutcliffe C, Langdon G, et al. The quasi-static and blast response of lattice structures. Int J Impact Eng 2008;35:795–810.
[11] Tsopanos S, Mines RAW, McKown S, Shen Y, Cantwell WJ, Brooks W, et al. The quasi-static and blast response of lattice structures. J Manuf Sci Eng 2010;132:0410111–12.
[12] Ushijima K, Cantwell WJ, Mines RAW, Tsupanos S, Smith M. An investigation into the compressive properties of stainless steel micro-lattice structures. J Sandwich Struct Mater 2011;13:303–29.
[13] Ushijima K, Cantwell WJ, Chen DH. Shear response of three-dimensional micro-lattice structures. Key Eng Mater 2011;452–453:303–29.
[14] Brettain ST, Sugimura Y, Schueller OLA, Evans AG, Whitesides GM. Fabrication and mechanical performance of a mesoscale space-filling truss system. J Microelectromechanical Syst 2002;10:113–120-329.
[15] Deshpande VS, Fleck NA, Ashby MF. Effective properties of the octet-truss lattice material. J Mech Phys Solids 2001;49:1747–69.
[16] Deshpande VS, Fleck NA. Collapse of truss core sandwich beams in 3-point bending. Int J Solids Struct 2001;38:6275–305.
[17] Wallach JC, Gibson LJ. Mechanical behavior of a three-dimensional truss material. Int J Solids Struct 2001;38:7181–96.
[18] Sypeck DJ, Wadley HNG. Cellular metal truss core sandwich structures. Adv Eng Mater 2002;4:759–64.
[19] Queheillalt DT, Wadley HNG. Cellular metal lattices with hollow trusses. Acta Mater 2005;53:303–13.
[20] Cote F, Deshpande VS, Fleck NA, Evans AG. The compressive and shear responses of corrugated and diamond lattice materials. Int J Solids Struct 2006;43:6220–42.
[21] Mines RAW. On the characterization of foam and micro-lattice materials used in sandwich construction. Strain 2008;44:71–83.
[22] Shaedler TA, Jacobsen AJ, Torrents A, Sorensen AE, Lian J, Greer JR, et al. Ultralight metallic microstructures. Science 2011;334:962–5.
[23] Love AEH. A treatise on the mathematical theory of elasticity. 4th ed. New York: Dover Publications; 2011.
[24] MSC Software. Marc 2010 manual, vols. A–E. MSC Software, California; 2010.
[25] Timoshenko SP, Gere JM. Theory of elastic stability. 2nd ed. New York: McGraw-Hill; 1961.